scientific reports

OPEN

Mesoscopic theory of defect ordering–disordering transitions in thin oxide films

Anna N. Morozovska[1], Eugene A. Eliseev[2], Dmitry V. Karpinsky[3], Maxim V. Silibin[4,5], Rama Vasudevan[6], Sergei V. Kalinin[6✉] & Yuri A. Genenko[7✉]

Ordering of mobile defects in functional materials can give rise to fundamentally new phases possessing ferroic and multiferroic functionalities. Here we develop the Landau theory for strain induced ordering of defects (e.g. oxygen vacancies) in thin oxide films, considering both the ordering and wavelength of possible instabilities. Using derived analytical expressions for the energies of various defect-ordered states, we calculated and analyzed phase diagrams dependence on the film-substrate mismatch strain, concentration of defects, and Vegard coefficients. Obtained results open possibilities to create and control superstructures of ordered defects in thin oxide films by selecting the appropriate substrate and defect concentration.

Ferroelectric and multiferroic materials are the object of much fascination in physics community, both due to the multitude of possible applications and broad spectrum of fundamental physical phenomena they exhibit. Applications such as ferroelectric memories, field effect transistors, and domain wall conductance have riveted attention of scientific community in the last two decades[1–3]. Similarly, the nature of ferroelectric transitions, ferroelectricity in disordered systems, etc. remain a subject of active research since the discovery of ferroelectricity in late 1920s[4]. Topological defects in ferroelectric materials and coupling between the ferroelectric and semiconductor subsystems are actively explored in the context of surface and domain wall conductance[5–8].

From the gamut of possible behaviors, in the last decade progressively more attention is focused on multiferroic materials, i.e. systems possessing two or more order parameters[9–12]. These functionalities significantly broaden the spectrum of possible applications, including oxide nanoelectronics, sensors and actuators, and IoT devices[13–16]. Furthermore, in multiferroic materials fundamentally new properties can emerge at the topological defects[17]. Examples of the former include the emergence of suppressed order parameter and associated topological defects at the domain walls, surfaces and interfaces, domain wall and vortex core conduction, incipient ferroelectricity and magnetism, and many others[8,18,19]. Remarkably that conductive domain walls in bulk samples and thin films can act as mobile charged channels (being also mobile topological defects) opening the way for "domain wall nanoelectronics"[20]. Additional degrees of functionality of nanosized multiferroics with the topological defects[11,21] and newly discovered low-dimensional semiconductor materials come from the strain engineering and straintronics concept[22].

The vast majority of the research in the field explored the coupling between the primary physical order parameters including magnetization, polarization, and ferroelasticity[8,18]. However, it is well known that chemical degrees of freedom can strongly affect the ferroic behavior[23]. A number of groups explored the phenomena such as vacancy segregation at the domain walls and grain boundaries[24–28], or changes in surface reactivity in response to polarization[29,30]. However, most of these works explore the responses of chemical subsystems to the polarization. Relatively small effort was dedicated to the exploration of chemical effects on polarization[31–33], typically the surface electrochemistry including chemically-induced switching[34–37] and emergence of ferroionic phases[38–40]. This direction has acquired particular prominence with the advent of the hybrid perovskites where

[1]Institute of Physics, National Academy of Sciences of Ukraine, 46, pr. Nauky, Kyiv 03028, Ukraine. [2]Institute for Problems of Materials Science, National Academy of Sciences of Ukraine, Krjijanovskogo 3, Kyiv 03142, Ukraine. [3]Scientific-Practical Materials Research Centre of NAS of Belarus, 220072 Minsk, Belarus. [4]National Research University of Electronic Technology "MIET", Moscow, Russia 124498. [5]Institute for Bionic Technologies and Engineering, I.M. Sechenov First Moscow State Medical University, Moscow, Russia 119991. [6]The Center for Nanophase Materials Sciences, Oak Ridge National Laboratory, Oak Ridge, TN 37922, USA. [7]Institute of Materials Science, Technische Universität Darmstadt, Otto-Berndt-Str.3, Darmstadt, Germany. ✉email: sergei2@ornl.gov; genenko@mm.tu-darmstadt.de
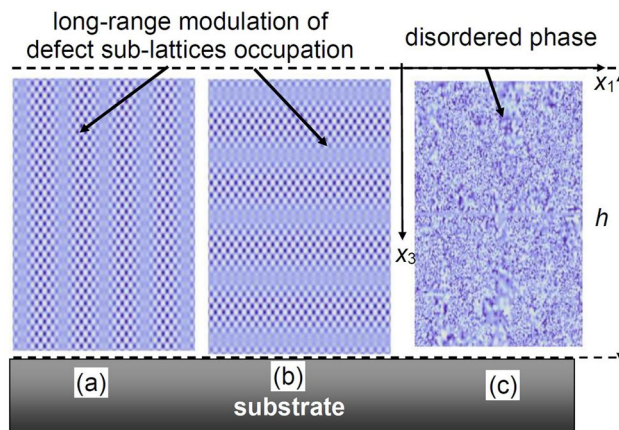
Figure 1. Point defect ordering in ultra-thin oxide film of thickness h placed on a rigid substrate. One can distinguish perpendicular (**a**, the left side) and parallel (**b**, the central part) orientations of the defect ordering from the state with randomly distributed defects (**c**, the right side). Parts (**a**) and (**b**) illustrate how the harmonic modulations of the order parameter reveal local redistribution of defects between defect sublattices.

chemical subsystem is strongly coupled to the environment and electrode phenomena (see e.g. review[41] and refs therein). However, the volume of research in this field is limited.

Here, we develop an initial framework for mesoscopic theory of defect ordering-disordering transitions in thin oxide films. We explore whether chemically induced changes in Vegard volume can be used to trigger and control multiferroic orderings in thin strained films (see e.g. Ref.[11,21,22] and refs. therein), and what are the properties of such systems.

Two sub-lattices model of point defects ordering

Here we consider the case of a thin oxide film on a substrate, taking into account the misfit strain[42], while neglecting the appearance of misfit dislocations. This assumption is generally valid for the films with a thickness smaller than a critical value (~ 10–50 nm) corresponding to dislocation nucleation[43]. The geometry of the problem is shown in Fig. 1. For high enough concentration of neutral/charged vacancies, the vacancy-ordered state can emerge[44] leading to the appearance of an elastic/electric dipole sublattice.

Rigorously speaking, in complex oxides there may be more than two oxygen sublattices[45]. However, our simplified continuum model with a scalar order parameter is naturally limited to two sublattices. The suggested model is isotropic in the $\{x_1, x_2\}$ plane together with the misfit strain. Since the symmetry breaking may spontaneously occur along any in-plane direction, this model is able to describe, particularly, a possible oxygen vacancy ordering along the x_1 or the x_2 axis. Thanks to the model symmetry, it is sufficient to consider exemplary cases of ordering along the x_1 axis, corresponding to the in-plane order parameter modulation, and along the x_3 axis, corresponding to the order parameter modulation perpendicular to the film surfaces.

The spatial scale of the defect concentration fluctuations, which can be correctly considered in a continuum approach, should be much larger than the lattice constant (so called long-range fluctuations). Thus, to describe the phase ordering process, we introduce a dimensionless long-range order parameter η, related to the degree of ordering of point defects (oxygen or cation vacancies, or impurity atoms) and given by a disbalance of occupations δn_a and δn_b of the two sub-lattices: $\eta = \frac{c}{c_0}(\delta n_b - \delta n_a)$. Here c is the concentration of defects related with the non-stoichiometry degree ξ; c_0 is a characteristic value that usually coincides with the solubility limit, meaning that the defect atoms do not affect essentially the host lattice force matrix at $c < c_0$. As one can see, the scalar order parameter η is a normalized occupation degree of the sub-lattices, $0 \leq |\eta| \leq 1$. For given η, the relative occupation numbers for the two sub-lattices are $\delta n_a = c(1 - \eta)/(2c_0)$ and $\delta n_b = c(1 + \eta)/(2c_0)$. The total occupation of two sub-lattices is constant, $\delta n_a + \delta n_b = c/c_0$. Values $\eta = \pm 1$ correspond to the complete ordering of defects in either sub-lattice "b" or "a", while $\eta = 0$ corresponds to the complete disorder (with equal filling of two sub-lattices).

Note that $c_0 < N_a$, where N_a is the stoichiometric concentration of host atoms. In the particular case of oxygen vacancies, c depends on the oxygen pressure p via the defect equilibria and for certain cases $\frac{c}{c_0} \sim \xi \sim ln\left(\frac{p_0 + A(T)p}{p_0}\right)$

(e.g. see Fig. 3 in Ref.[46]). Following the theory by Khachaturyan[47], we assume that concentration c is coordinate-independent.

The defect ordering direction can be different with respect to the film surfaces. Below we will distinguish perpendicular [see the left side (a) in Fig. 1] and parallel [see the central part (b) in Fig. 1] orientations of the planes of a constant order parameter and, thus, of equal sublattice occupations.

The η-dependent free energy of a thin film is the sum of the surface and bulk energies:

$$F = F_S + F_V, F_S = \frac{\alpha_S}{2} \int_{S_F} \left[\eta^2(x_1, x_2, 0) + \eta^2(x_1, x_2, h)\right] dx_1 dx_2, F_V = \int_{V_F} f dx_1 dx_2 dx_3 \quad (1a)$$

where h is the film thickness, and the first term is the surface/interface energy that is not negative under the condition $\alpha_S \geq 0$. Hereinafter we will consider the case $\alpha_S = 0$, corresponding to the so-called natural boundary conditions.

The bulk density, f, of the Helmholtz free energy dependence on the order parameter η has the form:

$$
\begin{aligned}
f(x_1, x_2, x_3) = {} & c^2 \frac{\alpha}{2} \eta^2 + \frac{c k_B T}{2}[(1 - \eta) \ln(1 - \eta) + (1 + \eta) \ln(1 + \eta)] \\
& + c^2 \frac{g_{kl}}{2} \frac{\partial \eta}{\partial x_k} \frac{\partial \eta}{\partial x_l} + c^2 \frac{w_{ijkl}}{2} \frac{\partial^2 \eta}{\partial x_i \partial x_j} \frac{\partial^2 \eta}{\partial x_k \partial x_l} + q[\eta, \sigma_{ij}]
\end{aligned}
\tag{1b}
$$

The first term in Eq. (1b), proportional to η^2, originates from the interaction between defects from the different sublattices. The term can be readily derived from the term $\delta n_a \delta n_b$ where δn_a and δn_b are the relative occupation numbers for the two sub-lattices. Hereinafter we will consider both cases $\alpha < 0$ and $\alpha > 0$. For the former, defects may order spontaneously in a bulk material, while in the latter case the ordering in bulk is unfavorable, but can be induced by external factors (such as misfit strain).

The second term in Eq. (1b) is proportional to the entropy of the system with a minus sign, $-TS$[42,44], since $F = U - TS$. The relative dimensionless entropy, defined as $-(1 - \eta)\ln(1 - \eta) - (1 + \eta)\ln(1 + \eta)$, tends to the minimum of $-2\ln 2$ under the condition $\eta^2 \to 1$, corresponding to the complete occupation of one of the sublattices ($\delta n_b = 1$ and $\delta n_a = 0$, or vice versa $\delta n_a = 1$ and $\delta n_b = 0$). We note that the entropy contribution stabilizes the system thermodynamically since its expansion contains all positive even powers of the order parameter.

The third and the fourth terms are the series expansion of generalized gradient energy in the derivatives $\partial \eta / \partial x_i$ of the order parameter. The gradient energy was introduced by Cahn and Hillard in 1958 (see e.g.[48]), since its inclusion becomes indispensable for correct description of inhomogeneous electrochemical systems with defect species. Below we consider the tensors g_{ij} and w_{ijkl} in isotropic approximation, $g_{ij} = g\delta_{ij}$ and $w_{ijkl} = w\delta_{ij}\delta_{kl}$, and explore the case of $w > 0$. This choice is because we study the case of the defects ordering for positive correlation energy.

Note that very often the higher gradient term is neglected ($w = 0$). Rigorously it is justified only if $g > 0$, assuming that its renormalization by the strain gradient energy is either positive or too small to change the positive sign of resulting effective gradient coefficient. Below we will show that w-term is mandatory to determine the threshold for emergence of the order parameter spatial modulation.

The elastic energy $q[\eta, \sigma_{ij}]$ includes the coupling between the order parameter and the stresses σ_{ij}. Following the theoretical formalism of Vegard strains, proposed by Freedman[49], and using the strain energy by Levanyuk et al.[50], the coupling term between the order parameter and the stresses could be also expanded as a series on the order parameter:

$$
\begin{aligned}
q[\eta, \sigma_{ij}] & = -\frac{s_{ijkl}}{2} \sigma_{ij}\sigma_{kl} + u_{ij}\sigma_{ij} - c_0 \sigma_{ij}\left(V_{ij}^{(a)}\delta n_a + V_{ij}^{(b)}\delta n_b\right) - c^2 \frac{B_{ijkl}}{2} \sigma_{ij} \frac{\partial \eta}{\partial x_k} \frac{\partial \eta}{\partial x_l} \\
& = -\frac{s_{ijkl}}{2} \sigma_{ij}\sigma_{kl} + u_{ij}\sigma_{ij} - c\left(V_{ij}^c + \eta V_{ij}^\eta\right)\sigma_{ij} - c^2 \frac{B_{ijkl}}{2} \sigma_{ij} \frac{\partial \eta}{\partial x_k} \frac{\partial \eta}{\partial x_l}
\end{aligned}
\tag{1c}
$$

here s_{ijkl} is the elastic compliances tensor, and u_{ij} is the tensor of elastic strains. To describe the mixed mechanical state of the epitaxial binary oxide film on the substrate, we perform the Legendre transform by adding the term $u_{kl}\sigma_{kl}$. The third term in Eq. (1c) is the chemical expansion due to the appearance of elastic defects, $c_0 \sigma_{ij}\left(V_{ij}^{(a)}\delta n_a + V_{ij}^{(b)}\delta n_b\right)$, where the tensors $V_{ij}^{(a)}$ and $V_{ij}^{(b)}$ characterize the Vegard strains for defects located within the sublattices (a) and (b), respectively. The symmetry of $V_{ij}^{(a,b)}$ is determined by the local site symmetry of defect with respect to the lattice, which could be different from the lattice symmetry (see e.g. Ref.[49] considering different vacancies in SrTiO$_3$). Using the expressions of the partial sublattice occupation numbers through the order parameter η the third term in Eq. (1c) can be further transformed to $c\left(V_{ij}^c + \eta V_{ij}^\eta\right)$ with the mean value $V_{ij}^c = \left(V_{ij}^{(a)} + V_{ij}^{(b)}\right)/2$ and the difference $V_{ij}^\eta = \left(V_{ij}^{(b)} - V_{ij}^{(a)}\right)/2$.

It will be shown that the last term in Eq. (1c) plays a central role in the mechanism of defect ordering. It is a gradient-type striction due to the defect ordering that is characterized by a fourth rank tensor B_{ijkl}.

In the continuous media approximation, the thermodynamically stable state of the film can be derived from the variation of the free energy (1) on η and σ_{ij}, leading to the Euler–Lagrange differential equations:

$$
\begin{aligned}
& \alpha c^2 \eta + c k_B T \, \mathrm{arctanh}(\eta) + c^2 B_{ijkl} \frac{\partial \sigma_{ij}}{\partial x_k} \frac{\partial \eta}{\partial x_l} \\
& - c^2 \left(g_{kl} - B_{ijkl}\sigma_{ij}\right) \frac{\partial^2 \eta}{\partial x_k \partial x_l} + \frac{c^2 w_{ijkl} \partial^4 \eta}{\partial x_i \partial x_j \partial x_k \partial x_l} - c V_{ij}^\eta \sigma_{ij} = 0
\end{aligned}
\tag{2a}
$$

$$
c\left(V_{ij}^c + \eta V_{ij}^\eta\right) + c^2 \frac{B_{ijkl}}{2} \frac{\partial \eta}{\partial x_k} \frac{\partial \eta}{\partial x_l} + s_{ijkl}\sigma_{kl} = u_{ij}
\tag{2b}
$$

here we used the identity, $\mathrm{arctanh}(\eta) \equiv \frac{1}{2}\ln\left(\frac{1+\eta}{1-\eta}\right)$.

The boundary conditions to Eq. (2a) are the following:

$$\left[\alpha_S \eta \pm gc^2 \frac{\partial \eta}{\partial z} \mp B_{ij33}\sigma_{ij}c^2 \frac{\partial \eta}{\partial z}\right]\Bigg|_{x_3=0,h} = 0. \tag{2c}$$

The first term in Eq. (2c) originated from the variation of surface energy in Eq. (1a), and the so-called natural boundary conditions correspond to the case $\alpha_S = 0$ (surface energy is absent in this particular case). The second term in Eq. (2c) originated from the variation of the gradient energy in Eq. (1b), and the third term originated from the variation of the elastic energy Eq. (1c).

Equation (2b) should be considered along with the conditions of mechanical equilibrium $\partial \sigma_{ij}/\partial x_j = 0$. The elastic boundary conditions to Eq. (2b) are the following:

$$\sigma_{i3}(x_1, x_2, 0) = 0, u_{11}(x_1, x_2, h) = u_{22}(x_1, x_2, h) = u_m. \tag{2d}$$

The first condition, $\sigma_{i3} = 0$, means that the top surface of the film ($x_3 = 0$) is mechanically free; and the second condition, $u_{11} = u_{22} = u_m$, means that the bottom surface of the film ($x_3 = h$) is clamped to a rigid substrate, where u_m is a misfit strain induced by the film-substrate lattices mismatch.

Below we consider thicknesses h smaller than the critical thickness of misfit dislocation appearance[43], typically this means that $h \lesssim 10$ nm.

The nonlinear boundary problem (2) contains a number of material-dependent constants, the majority of which are poorly known even for simple binary oxides, such as ZnO, MgO, SnO$_2$, CeO$_2$, HfO$_2$, and even more so for complex ternary oxides, such as manganites (La,Sr)MnO$_3$, paraelectric perovskites SrTiO$_3$, EuTiO$_3$, KTaO$_3$, ferroelectric perovskites (Ba,Sr)TiO$_3$, (Pb,Zr)TiO$_3$, and orthoferrites PbFeO$_3$, pristine and rare-earth doped BiFeO$_3$, etc., which all can be deficient in oxygen. Hence, prior to solving the boundary problem (2) by e.g. finite element modeling (FEM), requiring all tabulated parameters, these should be taken from the experimental or density functional studies[5,6,8,19]. However, to facilitate the search in the multi-parameter space and open the way for further FEM, here we elaborate the analytical theory.

Analytical solution in harmonic approximation

To explore the phase evolution in the system described by the free energy, Eq. (1), we consider the three-dimensional Fourier series of the order parameter,

$$\eta(\boldsymbol{x}) = \sum_{l,m,n=-\infty}^{\infty} \tilde{\eta}_{lmn} \exp\left[i\left(k_1^{(lmn)}x_1 + k_2^{(lmn)}x_2 + k_3^{(lmn)}x_3\right)\right], \tag{3a}$$

where the wave vector components $\boldsymbol{k}^{lmn} = \left(\frac{2\pi}{L}l, \frac{2\pi}{L}m, \frac{2\pi}{h}n,\right)$ are determined by the sizes $L \times L \times h$ of the considered film, and m, n, and l are integer numbers. For the order parameter $\eta(\boldsymbol{x})$ to be a real (i.e. observable) value, the equality $\tilde{\eta}_{l,m,n}^* = \tilde{\eta}_{-l,-m,-n}$ should be valid.

Following Landau theory, below we assume that only one principal mode **k** dominates near the order–disorder phase transition,

$$\eta(\boldsymbol{x}) \cong \eta_0 + \tilde{\eta}\exp(i\boldsymbol{k}\boldsymbol{x}) + c.c. \equiv \eta_0 + 2|\tilde{\eta}|\cos[(\boldsymbol{k}\boldsymbol{x} + \delta)], \tag{3b}$$

where δ is the phase shift and η_0 is the offset term. Next, we assume that the approximate equality is valid for the order parameter derivative in Eq. (1c), namely:

$$\frac{\partial \eta}{\partial x_m}\frac{\partial \eta}{\partial x_n} \cong 2k_m k_n \left|\tilde{\eta}\right|^2 (1 - \cos[2(\boldsymbol{k}\boldsymbol{x} + \delta)]) \tag{3c}$$

Note that **k** is constant in the first harmonic approximation, but should be found in the self-consistent way in what follows.

Substitution of Eq. (3) in Eqs. (1b) and (1c) yields:

$$\frac{g_{ij}c^2}{2}\frac{\partial \eta}{\partial x_i}\frac{\partial \eta}{\partial x_j} \cong c^2\tilde{g}|\tilde{\eta}|^2(1 - \cos[2(\boldsymbol{k}\boldsymbol{x} + \delta)]), \tag{4a}$$

$$\frac{B_{ijmn}}{2}\sigma_{ij}c^2 \frac{\partial \eta}{\partial x_m}\frac{\partial \eta}{\partial x_n} \cong c^2\tilde{B}_{ij}(\boldsymbol{k})\sigma_{ij}|\tilde{\eta}|^2(1 - \cos[2(\boldsymbol{k}\boldsymbol{x} + \delta)]), \tag{4b}$$

$$\frac{w_{ijkl}c^2}{2}\frac{\partial^2 \eta}{\partial x_i \partial x_j}\frac{\partial^2 \eta}{\partial x_k \partial x_l} \cong c^2\tilde{w}|\tilde{\eta}|^2(1 + \cos[2(\boldsymbol{k}\boldsymbol{x} + \delta)]), \tag{4c}$$

where $\tilde{g}(\boldsymbol{k}) = g_{ij}k_ik_j$, $\tilde{B}_{ij}(\boldsymbol{k}) = B_{ijmn}k_mk_n$ and $\tilde{w}(\boldsymbol{k}) = w_{ijmn}k_ik_jk_mk_n$.

Symmetry of the gradient-striction tensor B_{ijkl} is determined by the local site symmetry of defect with respect to the lattice. Below we assume the tetragonal symmetry of the tensor $B_{ij}(\boldsymbol{k})$, with a tetragonal axis along x_3 axis of the film.

In the continuum approximation, the thermodynamically stable state of the film can be analyzed by the variation of the free energy (1) that acquires the form:

$$F = \int_{V_F} dx \left[\frac{\alpha}{2}c^2\eta^2 + c\frac{k_B T}{2}[(1-\eta)\ln(1-\eta) + (1+\eta)\ln(1+\eta)] - \sigma_{ij}c\left(V_{ij}^c + V_{ij}^\eta\left(\eta_0 + 2\left|\tilde{\eta}\right|\cos[(\boldsymbol{kx}+\delta)]\right)\right) \right.$$
$$\left. -\frac{s_{ijkl}}{2}\sigma_{ij}\sigma_{kl} + u_{kl}\sigma_{kl} + c^2 \tilde{g}(\boldsymbol{k})\left|\tilde{\eta}\right|^2(1-\cos[2(\boldsymbol{kx}+\delta)]) + c^2 \tilde{w}(\boldsymbol{k})\left|\tilde{\eta}\right|^2(1+\cos[2(\boldsymbol{kx}+\delta)]) \right.$$
$$\left. -c^2\tilde{B}_{ij}(\boldsymbol{k})\sigma_{ij}\left|\tilde{\eta}\right|^2(1-\cos[2(\boldsymbol{kx}+\delta)]) \right]$$

(5a)

As a next step, one can use a Galerkin procedure in the free energy (5a) with respect to the second harmonics assuming statistical averaging, equivalent to the spatial averaging in ergodic case. Such averaging "excludes" the contributions from the second and higher harmonics to $\cos[2(\boldsymbol{kx}+\delta)]^{2n+1}$ due to a periodicity of trigonometric functions. Assuming the absence of correlations between the offset term η_0 and $\cos[2(\boldsymbol{kx}+\delta)]$, all cross-terms proportional to $\eta_0^{2m+1}\cos[2(\boldsymbol{kx}+\delta)]^{2n+1}$ vanish after the averaging. Next, the terms proportional to η_0^{2m+1} also vanish, while the even terms η_0^{2m} do not contain any useful information about defect ordering. Thus, one can regard that $\langle\eta^2\rangle \sim \left|\tilde{\eta}\right|^2 \sim \eta^2$, where the brackets $\langle...\rangle$ designate the averaging, and obtain:

$$\langle f \rangle \sim \frac{\alpha}{2}c^2\eta^2 + c\frac{k_B T}{2}[(1-\eta)\ln(1-\eta) + (1+\eta)\ln(1+\eta)]$$
$$- c\left(V_{ij}^c + \eta_0 V_{ij}^\eta\right)\sigma_{ij} - \frac{s_{ijkl}}{2}\sigma_{ij}\sigma_{kl} + u_{kl}\sigma_{kl} + c^2\tilde{g}(\boldsymbol{k})\eta^2 + c^2\tilde{w}(\boldsymbol{k})\eta^2 - c^2\tilde{B}_{ij}(\boldsymbol{k})\sigma_{ij}\eta^2$$

(5b)

Minimization of (5b), $\frac{\partial \langle f \rangle}{\partial \eta} = 0$ and $\frac{\partial \langle f \rangle}{\partial \sigma_{ij}} = 0$, instead of the Euler–Lagrange Eq. (2), yields the algebraic equations of state:

$$c\left(\alpha + 2\tilde{g} + 2\tilde{w} - 2\tilde{B}_{ij}\sigma_{ij}\right)\eta + k_B T \text{arctanh}(\eta) = 0,$$

(6a)

$$c\left(V_{ij}^c + \eta_0 V_{ij}^\eta\right) + \tilde{B}_{ij}c^2\eta^2 + s_{ijkl}\sigma_{kl} = u_{ij},$$

(6b)

Near the phase transition, $\text{arctanh}(\eta) \approx \eta + \frac{\eta^3}{3}$ in Eq. (6a).

Assuming that the anisotropic Vegard tensor is diagonal (or at least can be diagonalized), that is true for many cases[49], one can write $V_{ij}^c = V_{ii}^c\delta_{ij}$ and $V_{ij}^\eta = V_{ii}^\eta\delta_{ij}$. Using this approximation, elastic solution for a thin oxide film on a rigid substrate is derived for cubic symmetry far from the structural domain walls. Zero components are $\sigma_{33} = \sigma_{13} = \sigma_{23} = \sigma_{12} = 0, u_{12} = u_{13} = u_{23} = 0$, and nonzero components are:

$$\sigma_{11} = \frac{u_m}{s_{11}+s_{12}} - \frac{s_{11}\left(V_{11}^c + \eta_0 V_{11}^\eta + \tilde{B}_{11}c\eta^2\right) - s_{12}\left(V_{22}^c + \eta_0 V_{22}^\eta + \tilde{B}_{22}c\eta^2\right)}{s_{11}^2 - s_{12}^2}c,$$

(7a)

$$\sigma_{22} = \frac{u_m}{s_{11}+s_{12}} - \frac{s_{11}\left(V_{22}^c + \eta_0 V_{22}^\eta + \tilde{B}_{22}c\eta^2\right) - s_{12}\left(V_{11}^c + \eta_0 V_{11}^\eta + \tilde{B}_{11}c\eta^2\right)}{s_{11}^2 - s_{12}^2}c,$$

(7b)

$$u_{11} = u_{22} = u_m,$$

(7c)

$$u_{33} = \left(V_{33}^c + \eta_0 V_{33}^\eta\right)c + \tilde{B}_{33}c^2\eta^2 + \frac{s_{12}}{s_{11}+s_{12}}\left[2u_m - \left(V_{11}^c + V_{22}^c + \eta_0 V_{11}^\eta + \eta_0 V_{22}^\eta\right)c - \left(\tilde{B}_{11} + \tilde{B}_{22}\right)c^2\eta^2\right].$$

(7d)

The convolutions $\tilde{B}_{11} = B_{11}k_1^2 + B_{12}(k_2^2 + k_3^2)$, $\tilde{B}_{22} = B_{11}k_2^2 + B_{12}(k_1^2 + k_3^2)$ and $\tilde{B}_{33} = B_{11}k_3^2 + B_{12}(k_1^2 + k_2^2)$ are included in Eq. (7), and the Voight notations for $B_{1111} \equiv B_{11}$ and $B_{1122} \equiv B_{12}$ are used hereinafter.

Note, that in a freestanding film the stresses are zero $\sigma_{ij} = 0$, and elastic strains are $u_{ij} = c\left(V_{ij}^c + \eta_0 V_{ij}^\eta\right) + \tilde{B}_{ij}c^2\eta^2$.

Below we will suppose that $\eta_0 = 0$ and introduce the designations.

$$V_m = V_{11}^c + V_{22}^c, V_n = V_{11}^c - V_{22}^c,$$

(7e)

where the sum V_m has the sense of partial molar volume, and the difference V_n reflects the anisotropy impact.

Defect order–disorder transition
Long-range ordering parallel to the film surfaces.
Here we consider the case when the only nonzero component of wave vector is k_3, meaning that the harmonic modulation of the long-range order parameter $\eta \sim \left|\tilde{\eta}\right|\cos[k_3 x_3 + \delta]$ looks like planes parallel to the film surfaces $x_3 = 0, h$ (see Fig. 3a, left). Since η is proportional to the difference of defect sub-lattice occupations $\delta n_a - \delta n_b$, this means the modulation of the sub-lattice occupation perpendicular to the film surfaces.

For the case the free energy density Eq. (1) has the following form (see Supplementary Materials):

$$f[\eta] = \alpha_p + \frac{\beta_{pr}}{2}c^2\eta^2 + \frac{\gamma_{pr}c^4}{12}\eta^4 + c\frac{k_BT}{2}[(1-\eta)\ln(1-\eta) + (1+\eta)\ln(1+\eta)] \tag{8a}$$

where the coefficients $\alpha_p = \frac{(2u_m - V_m c)^2}{4(s_{11} + s_{12})} + \frac{c^2 V_n^2}{4(s_{11} - s_{12})}$, $\beta_{pr} = \alpha + 2\left(\widetilde{g} + \widetilde{w}\right) - 2\widetilde{B}_{22}\frac{2u_m - V_m c}{s_{11} + s_{12}}$, $\gamma_{pr} = \frac{12\widetilde{B}_{22}^2}{s_{11} + s_{12}}$, and $\widetilde{B}_{22} = B_{12}k_3^2$, $\widetilde{g} = gk_3^2$ and $\widetilde{w} = wk_3^4$. We refer the case with subscript "**pr**".

Omitting the η-independent term α_p, the free energy density (8a) can be expanded in power series in η as

$$\delta f[\eta] \approx \left(\beta_{pr}c^2 + ck_BT\right)\frac{\eta^2}{2} + \left(\frac{\gamma_{pr}c^4 + ck_BT}{3}\right)\frac{\eta^4}{4}. \tag{8b}$$

The derivation of Eq. (8) is given in Supplementary Materials[51]. Note that the renormalized coefficient before η^4 should be positive to ensure the stability of the phase described by the free energy (8b), otherwise higher terms should be included in the expansion. Since $s_{11} > |s_{12}|$ for all elastically stable solids, the condition $\gamma_{pr} \geq 0$ is always valid.

The equilibrium values of the order parameter obtained from minimization of the energy (8b) and the corresponding free energy have the form:

$$\eta_S^{pr} = \pm\sqrt{-3\frac{\beta_{pr}c + k_BT}{\gamma_{pr}c^3 + k_BT}}, \delta f_{pr}\left[\eta_S^{pr}\right] = -\frac{3c}{4}\frac{\left(\beta_{pr}c + k_BT\right)^2}{\gamma_{pr}c^3 + k_BT}. \tag{8c}$$

Long-range order exists if $\beta_{pr}c + k_BT < 0$.

Long-range ordering perpendicular to the film surface. We further consider the case when the only nonzero component of the wave vector is k_1, , meaning that the harmonic modulation of the long-range order parameter $\eta \sim \left|\widetilde{\eta}\right|\cos[k_1 x_1 + \delta]$ looks like planes perpendicular to the film surfaces $x_3 = 0$, h (see Fig. 3a, middle). Since η is proportional to the difference of defect sub-lattice occupations $\delta n_a - \delta n_b$, this means the modulation of the sub-lattice occupations parallel to the film surfaces.

The free energy density f in Eq. (1b) of the oxide has the following form in this case:

$$f[\eta] = \alpha_p + \frac{\beta_{pp}}{2}c^2\eta^2 + \frac{\gamma_{pp}c^4}{12}\eta^4 + c\frac{k_BT}{2}[(1-\eta)\ln(1-\eta) + (1+\eta)\ln(1+\eta)] \tag{9a}$$

where $\beta_{pp} = \alpha + 2\left(\widetilde{g} + \widetilde{w} - \left(\widetilde{B}_{11} + \widetilde{B}_{22}\right)\frac{2u_m - V_m c}{2(s_{11} + s_{12})} + \left(\widetilde{B}_{11} - \widetilde{B}_{22}\right)\frac{V_n c}{2(s_{11} - s_{12})}\right)$ and $\gamma_{pp} = 6\frac{\left(\widetilde{B}_{11}^2 + \widetilde{B}_{22}^2\right)s_{11} - 2\widetilde{B}_{11}\widetilde{B}_{22}s_{12}}{\left(s_{11}^2 - s_{12}^2\right)}$ with $\widetilde{B}_{11} = B_{11}k_1^2$, $\widetilde{B}_{22} = B_{12}k_1^2$, $\widetilde{g} = gk_1^2$ and $\widetilde{w} = wk_1^4$. We denote this case with subscript "**pp**".

Omitting the η–independent term α_p, the free energy density (9a) can be expanded in powers of η as

$$\delta f[\eta] \approx \left(\beta_{pp}c^2 + ck_BT\right)\frac{\eta^2}{2} + \left(\frac{\gamma_{pp}c^4 + ck_BT}{3}\right)\frac{\eta^4}{4}. \tag{9b}$$

Note that the renormalized coefficient before η^4 should be positive, otherwise higher terms should be included in the expansion. Thus, the inequality $\gamma_{pp}c^4 + ck_BT > 0$ should be verified. Since $s_{11} > |s_{12}|$ for all elastically stable solids, and $\widetilde{B}_{11}^2 + \widetilde{B}_{22}^2 \geq 2\left|\widetilde{B}_{11}\widetilde{B}_{22}\right|$ the condition $\gamma_{pp} > 0$ is always valid, and so $\gamma_{pp}c^4 + ck_BT > 0$ at finite temperatures.

The equilibrium values of the order parameter obtained from minimization of the energy (9b) and corresponding energy have the form similar to Eq. (8c):

$$\eta_S^{pp} = \pm\sqrt{-3\frac{\beta_{pp}c + k_BT}{\gamma_{pp}c^3 + k_BT}}, \delta f_{pp}\left[\eta_S^{pp}\right] = -\frac{3c}{4}\frac{\left(\beta_{pp}c + k_BT\right)^2}{\gamma_{pp}c^3 + k_BT}. \tag{9c}$$

Long-range order exists if $\beta_{pp}c + k_BT < 0$. The derivation of Eq. (9) is given in Supplementary Materials[51].

Note that, in the ordered phases, elastic dipoles may become polar due to the surface-induced piezoelectric coupling that, in turn, originates from the inversion symmetry breaking near the film surfaces. At the same time, the out-of-plane polar phase is affected by the strong depolarization field originated from the sharp gradient of polarization decay away from the surfaces.

Structural phase diagrams. The temperatures of transitions between defect-disordered and defect-ordered phases for parallel and perpendicular orientations of the planes of a constant order parameter can be determined from equations

$$T_{pp}[u_m, c, k_1] = -\frac{\beta_{pp}c}{k_B} \equiv -\frac{c}{k_B}\left(\alpha + 2\left(gk_1^2 + wk_1^4\right) - k_1^2\frac{(B_{11} + B_{12})}{s_{11} + s_{12}}(2u_m - V_m c) + k_1^2\frac{V_n(B_{11} - B_{12})}{s_{11} - s_{12}}c\right), \tag{10a}$$
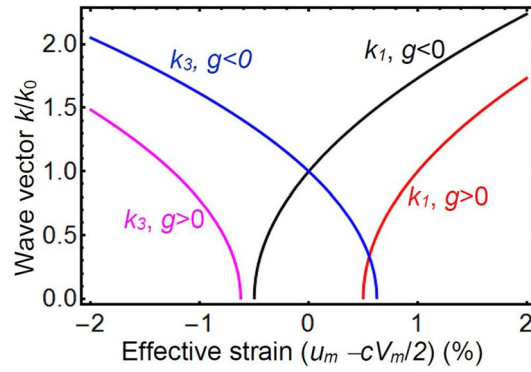
Figure 2. The dependence of the wave-vector component k_1/k_0 and k_3/k_0 on the effective strain $(u_m - cV_m/2)$ calculated from Eq. (11) for $g > 0$ (red and magenta curves) and $g < 0$ (black and blue curves), parameters $b_1 = 200$ and $b_3 = -160$.

$$T_{pr}[u_m, c, k_3] = -\frac{\beta_{pr}c}{k_B} \equiv -\frac{c}{k_B}\left(\alpha + 2\left(gk_3^2 + wk_3^4\right) - \frac{2k_3^2 B_{12}(2u_m - V_m c)}{s_{11} + s_{12}}\right). \tag{10b}$$

We further explore the equilibrium period of η-modulation, related to the wave vector $\boldsymbol{k}$. In equilibrium the conditions $\frac{\partial T_{pp}}{\partial k_i} = \frac{\partial T_{pr}}{\partial k_i} = 0$ should be fulfilled[52]. Thus $\frac{\partial T_{pp}}{\partial k_1} = -\frac{2c}{k_B}k_1\left(2g - \frac{(B_{11}+B_{12})(2u_m - V_m c)}{s_{11}+s_{12}}\right.$
$\left. + \frac{V_n(B_{11}-B_{12})}{s_{11}-s_{12}}c + 4wk_1^2\right) = 0$ for the constant η-planes perpendicular to the film surfaces, and $\frac{\partial T_{pr}}{\partial k_3} = -\frac{2c}{k_B}k_3\left(2g - 2B_{12}\frac{2u_m - V_m c}{s_{11}+s_{12}} + 4wk_3^2\right) = 0$ for the constant η-planes parallel to the film surfaces.

From these conditions the components of the modulation vector acquire the form:

$$k_1 = \pm\sqrt{-\frac{1}{4w}\left(2g - (B_{11}+B_{12})\frac{2u_m - cV_m}{s_{11}+s_{12}} + \frac{cV_n(B_{11}-B_{12})}{s_{11}-s_{12}}\right)}, \tag{11a}$$

$$k_3 = \pm\sqrt{-\frac{1}{2w}\left(g - \frac{B_{12}(2u_m - V_m c)}{s_{11}+s_{12}}\right)}. \tag{11b}$$

It is instructive to rewrite and analyze expressions (11) in a dimensionless form, namely $\frac{k_1}{k_0} = \pm\sqrt{-\frac{g}{|g|} - \frac{g_a}{|g|} + b_1 u}$ and $\frac{k_3}{k_0} = \pm\sqrt{-\frac{g}{|g|} + b_3 u}$, where $k_0 = \sqrt{\frac{|g|}{2w}}$ is a characteristic wave number, $u = u_m - cV_m/2$ is a dimensionless "effective" strain; $b_1 = \frac{B_{11}+B_{12}}{|g|(s_{11}+s_{12})}$ and $b_3 = \frac{2B_{12}}{|g|(s_{11}+s_{12})}$ are dimensionless gradient-related parameters. Below we will analyze the positive roots $k_{1,3} > 0$ only, since the negative ones describe the same physical states. Here we also introduced anisotropy term $g_a = (B_{11} - B_{12})\frac{cV_n}{2(s_{11}-s_{12})}$.

Figure 2 illustrates the square-root like dependences of the dimensionless wave-vector components, k_1/k_0 and k_3/k_0, on the effective strain u for $g > 0$ (red and magenta curves) and $g < 0$ (black and blue curves). Note that positive w determines the existence of the modulation and its characteristic wave number.

The transition temperatures, corresponding to the η-modulation vectors given by Eq. (11), are

$$T_{pp}(u_m, c) = -\frac{c}{k_B}\left[\alpha - \frac{1}{4w}\left(2g - (B_{11}+B_{12})\frac{2u_m - cV_m}{s_{11}+s_{12}} + (B_{11}-B_{12})\frac{cV_n}{s_{11}-s_{12}}\right)^2\right] \tag{12a}$$

$$T_{pr}(u_m, c) = -\frac{c}{k_B}\left[\alpha - \frac{1}{2w}\left(g - B_{12}\frac{2u_m - V_m c}{s_{11}+s_{12}}\right)^2\right] \tag{12b}$$

The conditions of the equilibrium between the ordered phases can be obtained from the equality of the corresponding free energy densities, Eqs. (8c) and (9c), namely.

$$\frac{\left(\beta_{pr}c + k_B T\right)^2}{\gamma_{pr}c^3 + k_B T} = \frac{\left(\beta_{pp}c + k_B T\right)^2}{\gamma_{pp}c^3 + k_B T}, \tag{13a}$$

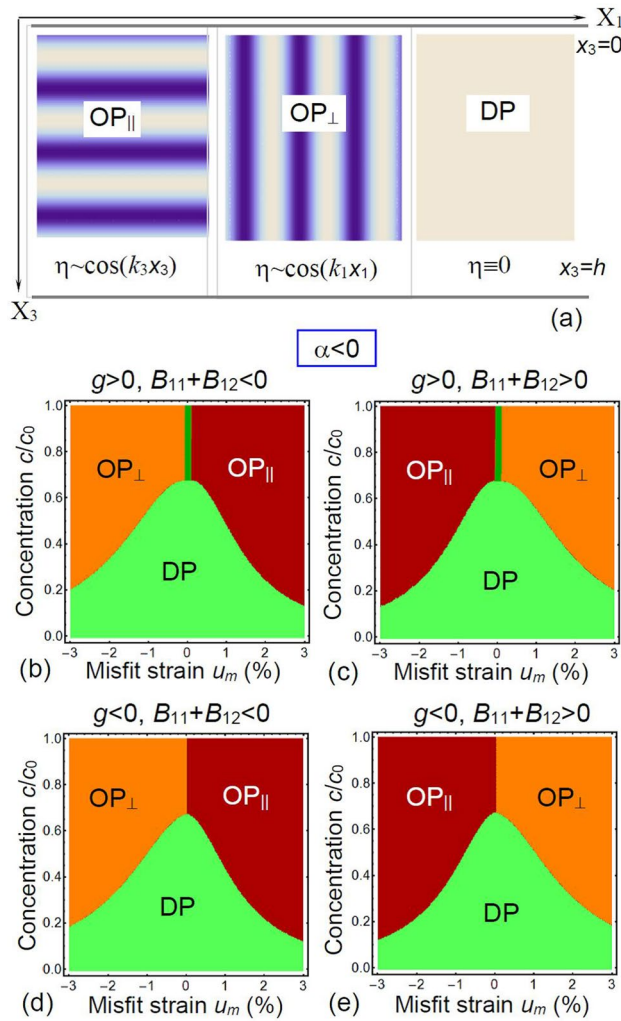allowing for the conditions of the long-range orders existence

Figure 3. (**a**) Geometry of the problem and schematics of different phases characterized by different directions of the order parameter η modulation. The $OP_\parallel$ phase is characterized by a periodic change $\eta \sim \left|\tilde{\eta}\right|\cos[k_3 x_3 + \delta]$ perpendicular to the substrate plane $x_3 = h$. The $OP_\perp$ phase is characterized by a periodic change $\eta \sim \left|\tilde{\eta}\right|\cos[k_1 x_1 + \delta]$ parallel to the substrate plane $x_3 = h$. The disordered DP phase is characterized by $\eta = 0$.

(**b**)–(**e**) Phase diagrams in dependence on the normalized defect concentration c/c_0 and misfit strain u_m calculated for negative α, different signs of coefficient g and striction coefficients B_{ij} (indicated above the plots) at room temperature T = 293 K. Parameters: $\alpha c_0^2 = -6 \times 10^4$ J m^{-3}, $|g| c_0^2 = 10^{-17}$ J/m, $w c_0^2 = 3 \times 10^{-37}$ J m, $s_{11} = 4 \times 10^{-12}$ Pa^{-1}, $s_{12} = -1 \times 10^{-12}$ Pa^{-1}, $V_m = 30$ Å^3, while striction coefficients $B_{11} c_0^2 = 5 \times 10^{-26}$ J m^2, and $B_{12} c_0^2 = -2 \times 10^{-26}$ J·m^2, and maximal (steric limit) concentration of defects is $c_0 = 10^{25}$ m^{-3}.

$$\beta_{pr} c + k_B T < 0, \beta_{pp} c + k_B T < 0. \tag{13b}$$

Note that the expressions (11) for **k**-vector components should be substituted in Eqs. (13).

Equation (13a) can be solved with respect to temperature in the following form:

$$T = \frac{c}{k_B} \frac{\left(\beta_{pr}^2 - \beta_{pp}^2\right) + 2c^2\left(\beta_{pr}\gamma_{pp} - \beta_{pp}\gamma_{pr}\right) \pm \text{Det}\left[\beta_{pp}, \beta_{pr}\right]}{4\left(\beta_{pp} - \beta_{pr}\right) - 2\left(\gamma_{pp} - \gamma_{pr}\right)c^2}, \tag{14a}$$

$$\text{Det}\left[\beta_{pp}, \beta_{pr}\right] = \sqrt{\left(\beta_{pp} - \beta_{pr}\right)^4 + 4\left(\beta_{pp} - \gamma_{pp}c^2\right)\left(\beta_{pr} - \gamma_{pr}c^2\right)\left(\beta_{pp} - \beta_{pr}\right)^2}. \tag{14b}$$

The signs "±" in Eq. (14a) correspond to two different roots, which have physical sense if correspond to $T \geq 0$. These roots should further satisfy two conditions (13b). Depending on the parameters it appeared possible at least for the largest root of Eq. (14a). Since the sign of denominator in Eq. (14a) is not fixed, both signs in the numerator, $+\text{Det}\left[\beta_{pp}, \beta_{pr}\right]$ or $-\text{Det}\left[\beta_{pp}, \beta_{pr}\right]$, are possible depending on the parameters. Hence, the number
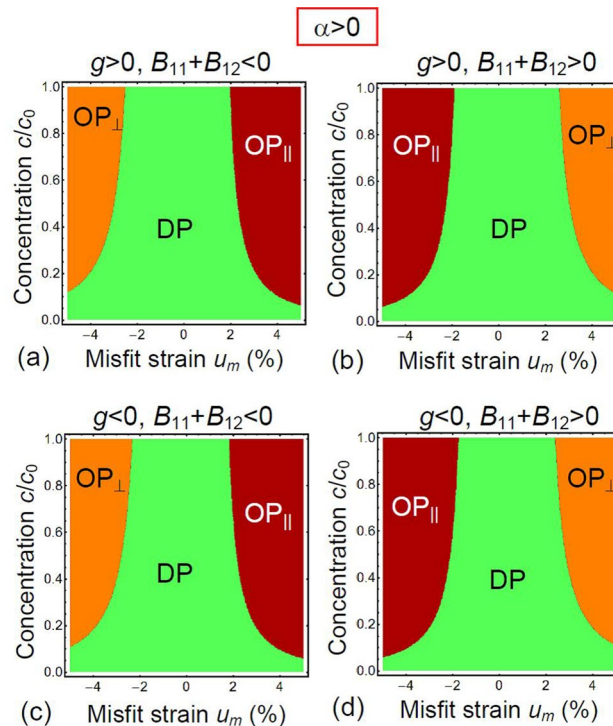
Figure 4. Phase diagrams in dependence on normalized defect concentration c/c_0 and misfit strain u_m calculated for different signs of gradient coefficient g and striction coefficients B_{ij} (indicated above the plots), and $\alpha > 0$. Other parameters are the same as in Fig. 3.

and selection of the roots in Eq. (14a) should be established numerically depending on the number and values of the fitting parameters.

It can be shown that, at the chosen parameter values, one of the roots (14a) is close to the expression $\left(T_{pp}(u_m, c) + T_{pr}(u_m, c)\right)/2$. Hence, for $\beta_{pp} \approx \beta_{pr}$ expression (14a) can be expanded in series on the small difference $\left(\beta_{pp} - \beta_{pr}\right)$ powers, namely

$$T \approx \frac{c}{k_B}\left(\beta_{pp} - \beta_{pr}\right)\left(-\frac{1}{2} + \frac{\gamma_{pp}c^2 - \beta_{pp} \pm \sqrt{\left(\gamma_{pp}c^2 - \beta_{pp}\right)\left(\gamma_{pr}c^2 - \beta_{pr}\right)}}{\left(\gamma_{pp} - \gamma_{pr}\right)c^2}\right). \tag{14c}$$

When a strong inequality $\left|\gamma_{pp} - \gamma_{pr}\right| << \gamma_{pp}$ takes place, the second term in parenthesis in Eq. (14c) could be either close to unity (sign "−") or much higher than unity (sign "+"). It is seen that in the case of sign "−" the solutions (14b)-(14c) will not satisfy both of relations (13b) simultaneously. The other root in Eq. (14a) deviates more significantly from the value $\left[T_{pp}(u_m, c) + T_{pr}(u_m, c)\right]/2$, thus, in this case, conditions (13b) will be satisfied.

Using Eqs. (10)-(14) we plotted phase diagrams of the system and corresponding modulation amplitudes and wave vectors, shown in Figs. 3, 4 and 5, respectively. Note that the ordered phases $OP_\perp$ and $OP_\parallel$ have different orientation of the order parameter modulation amplitude, $\eta(x_1)$ and $\eta(x_3)$, with respect to the film surfaces.

Figure 3a represents the scheme of the $\eta(x_1, x_3)$ distribution in the ordered ($OP_\perp$ and $OP_\parallel$) and disordered (DP) phases. The ordered phases $OP_\perp$ and $OP_\parallel$ are characterized by periodic changes of $\eta = \frac{c}{c_0}(\delta n_b - \delta n_a)$, which are proportional to the difference of the sublattices "a" and "b" occupation numbers, $\delta n_b - \delta n_a$. The total concentration "c" remains constant, since the sum $\delta n_a + \delta n_b$ is independent on η. The $OP_\parallel$ phase is characterized by a periodic change $\eta \sim \left|\tilde{\eta}\right|\cos[k_3 x_3 + \delta]$, corresponding to the long-range modulation of the defect sub-lattices "a" and "b" occupation perpendicular to the substrate plane $x_3 = h$. The $OP_\perp$ phase is characterized by a periodic change $\eta \sim \left|\tilde{\eta}\right|\cos[k_1 x_1 + \delta]$, corresponding to the long-range modulation of the defect sub-lattices "a" and "b" occupation parallel to the substrate plane $x_3 = h$. The disordered DP phase is characterized by $\eta = 0$, corresponding to the equal filling of both sub-lattices. Note that the modulation periods, $\frac{2\pi}{k_1}$ and $\frac{2\pi}{k_3}$, should be significantly larger than the lattice constant for the validity of the continuum approach, and so Fig. 3a illustrates only these long-range modulations of the order parameter $\eta(\boldsymbol{x})$, but not the distance between the defect sub-lattices planes.

Figures 3 and 4 are phase diagrams of an ultra-thin film in dependence on the misfit strain u_m and the dimensionless defect concentration c/c_0 calculated for negative and positive α, respectively. Corresponding modulation wave vectors, $k_\perp$ and $k_\parallel$, are shown in Fig. 5a,b, respectively.

Figure 3b–e, calculated for negative α, demonstrate the presence of $OP_\perp$, $OP_\parallel$ and DP phases, whose boundaries depend on the gradient g and striction B_{ij} coefficients, which are different for Fig. 3b–e. The ultrathin almost vertical dark green stripe between $OP_\parallel$ and $OP_\perp$ phases located at small $|u_m| < 0.1\%$ in Fig. 3b,c is the coexistence
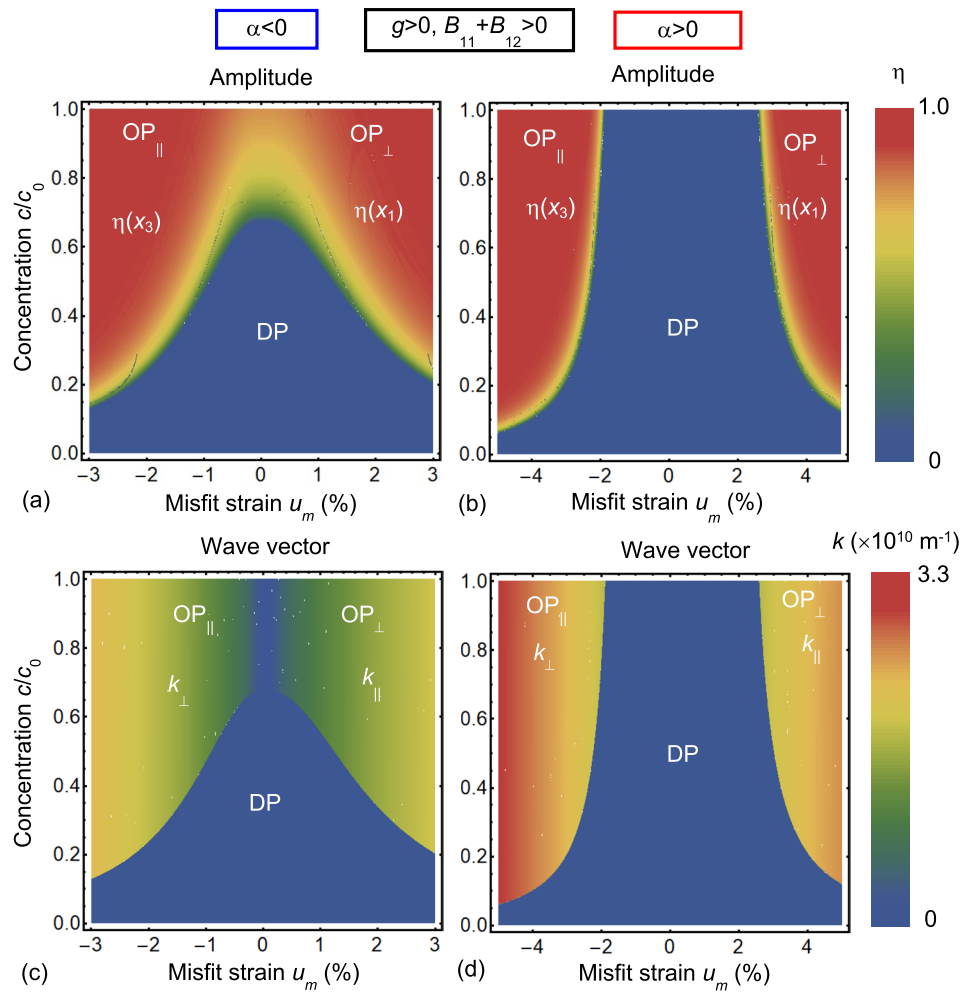
Figure 5. Order parameter amplitudes $\eta(x_1)$ and $\eta(x_3)$ (**a,b**) and wave vectors (**c,d**) in dependence on normalized defect concentration c/c_0 and misfit strain u_m calculated for negative α (**a,c**) and positive α (**b,d**); $g > 0$, and $B_{11} + B_{12} > 0$. Numerical values of parameters are the same as in Fig. 3.

region of the ordered phases, where the wave vector becomes very small, $k \to 0$. This phase is absent for the diagrams in Fig. 3d,e, which have a tricritical point, where $OP_\perp$, $OP_\parallel$ and DP phases coexist. The tricritical point $\{u_m = 0, c/c_0 = 0.63\}$ is almost independent on g and B_{ij} signs. The $OP_\parallel$-DP and $OP_\perp$-DP boundaries are curved for all diagrams. DP phase occupies mountain-shape region with the "top" at $\{u_m = 0, c/c_0 = 0.63\}$, which hill-sides start at small misfits. The region of its stability gradually decreases with $|u_m|$ increase. At that the noticeable asymmetry between compressive ($u_m < 0$) and tensile ($u_m > 0$) misfit strains is evident and related with positive Vegard effect ($V_m > 0$). It can be deduced from Fig. 3b–e, that the change of the B_{ij} sign leads to an interchange between the $OP_\parallel$ and $OP_\perp$ phases with different orientation of η-ordering, stemming from the chemo-strictive coupling between the strain u_m and defect concentration c, expressed by the coupling terms $\frac{B_{11}+B_{12}}{s_{11}+s_{12}}(u_m - cV_m/2)$ and $\frac{2B_{12}}{s_{11}+s_{12}}(u_m - cV_m/2)$.

The $OP_\parallel$-$OP_\perp$ boundary is almost vertical, and its small slope weakly depends on the V_m value. The $OP_\perp$ phase exists for compressive misfit strain $u_m < 0$ at $B_{11} + B_{12} < 0$, and for tensile misfit strain $u_m > 0$ at $B_{11} + B_{12} > 0$. The $OP_\parallel$ phase exists for compressive misfit strain $u_m < 0$ at $B_{11} + B_{12} > 0$, and for tensile misfit strain $u_m > 0$ at $B_{11} + B_{12} < 0$. The color maps of the order parameter amplitudes $[\eta(x_1)$ and $\eta(x_3)]$ and wave vectors ($k_\perp$ and $k_\parallel$) calculated for $\alpha < 0$, $g > 0$, $B_{11} + B_{12} > 0$ are shown in Fig. 5a,c, respectively. The continuous transition from $OP_\parallel$ to $OP_\perp$ phase occurs at $u_m = 0$. Notably that $k_\perp = k_\parallel = 0$ in the region $u_m \approx 0$. The values of η and k gradually increase with $|u_m|$ increase.

The change of α sign critically affects the phase diagrams, as is shown in Fig. 4. The most pronounced effect is the appearance of the wide DP region between the ordered $OP_\perp$ and $OP_\parallel$ phases, so that the tricritical point is absent for all concentrations "c". Note that the DP exists in the regions of misfits $|u_m| \leq 2\%$ and this region grows with defect concentration decrease. The width of the DP region slightly increases with $|u_m|$ increase. The change of the B_{ij} sign leads to the interchange between the $OP_\parallel$ and $OP_\perp$ phases, while the effect of the coefficient g is negligibly small in this case [compare Fig. 4a,b with 4c-d]. The $OP_\perp$ phase exists for high compressive misfit strain $u_m < -2.5\%$ at $B_{11} + B_{12} < 0$, and for tensile misfit strain $u_m > +2.5\%$ at $B_{11} + B_{12} > 0$. The $OP_\parallel$ phase

exists for compressive misfit strain $u_m < -1.9\%$ at $B_{11} + B_{12} > 0$, and for tensile misfit strain $u_m > +1.9\%$ at $B_{11} + B_{12} < 0$. The color maps of the order parameter amplitudes [$\eta(x_1)$ and $\eta(x_3)$] and wave vectors ($k_\perp$ and $k_\parallel$) calculated for $\alpha > 0$, $g > 0$, $B_{11} + B_{12} > 0$ are shown in Fig. 5b,d, respectively. The OP$_\parallel$ to OP$_\perp$ phases are separated by a wide region of the DP phase located at $|u_m| \leq 2\%$. The values of k are nonzero at the DP-OP$_\parallel$ and DP-OP$_\perp$ boundaries. The values of η and k gradually increase with $|u_m|$ increase.

Note that the values of the order parameter η and the components of the wave vector, k_1 and k_3, were calculated on the basis of numerical minimization of the more complex free energy functional [see Eqs. (8a) and (9a)], for which the series expansion was not used. It turned out that the differences between the approximate expressions (11) and the results of numerical calculations are insignificant for the wave vector. Also, to describe the phase transitions between the ordered and disordered phases, expressions (12) exactly correspond to numerical calculations, since these transitions are the second-order phase transitions and, the order parameter can be considered small near the transition points.

Note that phenomenological parameters listed in the caption to Fig. 3 were selected in such a way so as to satisfy the physical conditions $\alpha c_0 \cong k_B T_{room}$, $\sqrt{|\alpha|/g} \geq k_0$, $\sqrt{|g|/w} < k_0$, while s_{ij} and c_0 values are typical for oxides. As for the striction coefficients B_{ij}, these are chosen so that the combinations of parameters, $\frac{B_{11}+B_{12}}{s_{11}+s_{12}}(u_m - cV_m/2)$ and $\frac{2B_{12}}{s_{11}+s_{12}}(u_m - cV_m/2)$, are of the same order as $|g|$. To summarize the section, results shown in Fig. 3, 4 and 5 indicate that one can control the defect ordering-disordering by changing their concentration c/c_0 and misfit strain u_m at fixed values of the other parameters.

Finally it may be interesting to compare the defect ordering with the cycloid ordering in a strained multiferroic BiFeO$_3$ thin films (see e.g. Ref.[11,21,22] and refs. to original papers therein). Actually, the strain-induced singularity of the cycloid period and phase diagram with various spin cycloid orientations in BiFeO$_3$ can be topologically analogous to the one considered in Figs. 3, 4 and 5 proving that chiral incommensurate phases of defect ordering (allowed by the theoretical formalism) can exist in the strained film.

Conclusion

We have analyzed the ordering of defects (e.g. oxygen vacancies) in thin oxide films in the framework of the continuum Landau-type theory. We derived analytical expressions for the energies of various defect-ordered states and calculated and analyzed phase diagrams dependence on the film-substrate misfit strain and concentration of defects for different gradient, striction and Vegard coefficients.

We have found that two defect-ordered phases, which are characterized by either parallel or perpendicular defect ordering in planes and corresponding wave vectors, can be stable. The stability conditions are determined by the misfit strain and the defect concentration at fixed values of the other parameters. The ordered phases border with the defect-disordered phase. Hence, we have shown that it is possible to control the defect ordering-disordering by changing their concentration and the film-substrate misfit strain (compressive or tensile). Thus, the obtained results open possibilities to create and control superstructures of ordered defects in thin oxide films by selecting the appropriate substrate and defect concentration.

References

1. Scott, J. F. Data storage: multiferroic memories. *Nat. Mater.* **6**, 256–257 (2007).
2. Glinchuk, M. D., Ragulya, A. V. & Stephanovich, V. A. *Nanoferroics*. (Springer Series in Mater. Sci. **177**, 2013).
3. Sharma, P., Schoenherr, P. & Seidel, J. Functional ferroic domain walls for nanoelectronics. *Materials* **12**, 2927 (2019).
4. Valasek, J. Piezoelectric and allied phenomena in Rochelle salt. *Phys. Rev.* **17**, 475–481 (1921).
5. Balke, N. *et al.* Enhanced electric conductivity at ferroelectric vortex cores in BiFeO$_3$. *Nat. Phys.* **8**, 81–88 (2012).
6. Winchester, B. *et al.* Electroelastic fields in artificially created vortex cores in epitaxial BiFeO$_3$ thin films. *Appl. Phys. Lett.* **107**, 052903 (2015).
7. Morozovska, A. N., Eliseev E. A. & Kalinin, S. V. Topological defects in ferroic materials. In *Topological Structures in Ferroic Materials*, 181–197 (Springer Series in Mater. Sci. **228**, 2016).
8. Han, M. J. *et al.* Mapping gradient-driven morphological phase transition at the conductive domain walls of strained multiferroic films. *Phys. Rev. B* **100**, 104109 (2019).
9. Fiebig, M. Revival of the magnetoelectric effect. *J. Phys. D Appl. Phys.* **38**, R123 (2005).
10. Spaldin, N. A. & Fiebig, M. The renaissance of magnetoelectric multiferroics. *Science* **309**, 391–392 (2005).
11. Pyatakov, A. P. & Zvezdin, A. K. Magnetoelectric and multiferroic media. *Phys. Usp.* **55**, 557–581 (2012).
12. Fiebig, M., Lottermoser, T., Meier, D. & Trassin, M. The evolution of multiferroics. *Nat. Rev. Mater.* **1**, 16046 (2016).
13. Rondinelli, J. M. & Spaldin, N. A. Structure and properties of functional oxide thin films: insights from electronic structure calculations. *Adv. Mater.* **23**, 3363–3381 (2011).
14. Morozovska, A. N. *et al.* Flexocoupling impact on the size effects of piezo- response and conductance in mixed-type ferroelectrics-semiconductors under applied pressure. *Phys. Rev. B* **94**, 174101 (2016).
15. Seidel, J. Nanoelectronics based on topological structures. *Nat. Mater.* **18**, 188–190 (2019).
16. Hassanpour, E. *et al.* Interconversion of multiferroic domains and domain walls. Preprint at https://arxiv.org/abs/1908.06876 (2019).
17. Pyatakov, A. P. Magnetoelectricity goes local: from bulk multiferroic crystals to ferroelectricity localized on magnetic topological textures. *Phys. B* **542**, 59–62 (2018).
18. Eliseev, E. A., Morozovska, A. N., Nelson, C. T. & Kalinin, S. V. Intrinsic structural instabilities of domain walls driven by gradient couplings: meandering anferrodistortive-ferroelectric domain walls in BiFeO$_3$. *Phys. Rev. B* **99**, 014112 (2019).
19. Morozovska, A. N., Eliseev, E. A., Chen, D., Nelson, C. T. & Kalinin, S. V. Building free energy functional from atomically-resolved imaging: atomic scale phenomena in La-doped BiFeO$_3$. *Phys. Rev. B* **99**, 195440 (2019).
20. Catalan, G., Seidel, J., Ramesh, R. & Scott, J. F. Domain wall nanoelectronics. *Rev. Mod. Phys.* **84**, 119–156 (2012).
21. Sando, D. *et al.* Crafting the magnonic and spintronic response of BiFeO$_3$ films by epitaxial strain. *Nat. Mater.* **12**, 641–646 (2013).

22. Bukharaev, A. A., Zvezdin, A. K., Pyatakov, A. P. & Fetisov, Y. K. Straintronics: a new trend in micro-, nanoelectronics and material science. *Phys. Usp.* **61**, 1175–1212 (2018).
23. Eliseev, E. A. *et al.* Defect driven flexo-chemical coupling in thin ferroelectric films. *Phys. Rev. B* **97**, 024102 (2018).
24. Thomann, H. Stabilization effects in piezoelectric lead titanate zirconate ceramics. *Ferroelectrics* **4**, 141–146 (1972).
25. Genenko, Y. A. *et al.* Aging of poled ferroelectric ceramics due to relaxation of random depolarization fields by space-charge accumulation near grain boundaries. *Phys. Rev. B* **80**, 224109 (2009).
26. Froemling, T., Hutter, H. & Fleig, J. Oxide ion transport in donor-doped $Pb(Zr_xTi_{1-x})O_3$: near-surface diffusion properties. *J. Am. Ceram. Soc.* **95**, 1692–1700 (2012).
27. Sluka, T., Tagantsev, A. K., Bednyakov, P. & Setter, N. Free-electron gas at charged domain walls in insulating $BaTiO_3$. *Nat. Commun.* **4**, 1808 (2013).
28. Vorotiahin, I. S., Morozovska, A. N. & Genenko, Y. A. Hierarchy of domain reconstruction processes due to charged defect migration in acceptor doped ferroelectrics. *Acta Mater.* **184**, 267–283 (2020).
29. Kolpak, G. A. I. & Rappe, A. Polarization effects on the surface chemistry of $PbTiO_3$ -supported Pt films. *Phys. Rev. Lett.* **98**, 166101 (2007).
30. Chiu, Y.-H., Chang, K.-D. & Hsu, Y.-J. Plasmon-mediated charge dynamics and photoactivity enhancement for Au-decorated ZnO nanocrystals. *J. Mater. Chem. A* **6**, 4286–4296 (2018).
31. Highland, M. J. *et al.* Polarization switching without domain formation at the intrinsic coercive field in ultrathin ferroelectric PbTiO3. *Phys. Rev. Lett.* **105**, 167601 (2010).
32. Yang, S. M. *et al.* Mixed electrochemical-ferroelectric states in nanoscale ferroelectrics. *Nat. Phys.* **13**, 812–818 (2017).
33. Kalinin, S. V., Kim, Y., Fong, D. & Morozovska, A. N. Surface screening mechanisms in ferroelectric thin films and its effect on polarization dynamics and domain structures. *Rep. Prog. Phys.* **81**, 036502 (2018).
34. Wang, R. V. *et al.* Reversible chemical switching of a ferroelectric film. *Phys. Rev. Lett.* **102**, 047601 (2009).
35. Fong, D. D. *et al.* Stabilization of monodomain polarization in ultrathin $PbTiO_3$ films. *Phys. Rev. Lett.* **96**, 127601 (2006).
36. Highland, M. J. *et al.* Equilibrium polarization of ultrathin $PbTiO_3$ with surface compensation controlled by oxygen partial pressure. *Phys. Rev. Lett.* **107**, 187602 (2011).
37. Stephenson, G. B. & Highland, M. J. Equilibrium and stability of polarization in ultrathin ferroelectric films with ionic surface compensation. *Phys. Rev. B* **84**, 064107 (2011).
38. Morozovska, A. N., Eliseev, E. A., Morozovsky, N. V. & Kalinin, S. V. Ferroionic states in ferroelectric thin films. *Phys. Rev. B* **95**, 195413 (2017).
39. Morozovska, A. N., Eliseev, E. A., Morozovsky, N. V. & Kalinin, S. V. Piezoresponse of ferroelectric films in ferroionic states: time and voltage dynamics. *Appl. Phys. Lett.* **110**, 182907 (2017).
40. Morozovska, A. N. *et al.* Effect of surface ionic screening on polarization reversal scenario in ferroelectric thin films: crossover from ferroionic to antiferroionic states. *Phys. Rev. B* **96**, 245405 (2017).
41. Grancini, G. & Nazeeruddin, M. K. Dimensional tailoring of hybrid perovskites for photovoltaics. *Nat. Rev. Mat.* **4**, 4–22 (2019).
42. Pertsev, N. A., Zembilgotov, A. G. & Tagantsev, A. K. Effect of mechanical boundary conditions on phase diagrams of epitaxial ferroelectric thin films. *Phys. Rev. Lett.* **80**, 1988–1991 (1998).
43. Speck, J. S. & Pompe, W. Domain configurations due to multiple misfit relaxation mechanisms in epitaxial ferroelectric thin films. I. Theory. *J. Appl. Phys.* **76**, 466–476 (1994).
44. Borisevich, A. Y. *et al.* Exploring mesoscopic physics of vacancy-ordered systems through atomic scale observations of topological defects. *Phys. Rev. Lett.* **109**, 065702 (2012).
45. Nowick, A. S. & Heller, W. R. Anelasticity and stress-induced ordering of point defects in crystals. *Adv. Phys.* **12**, 251–298 (1963).
46. Chen, X., Yu, J. & Adler, S. B. Thermal and chemical expansion of Sr-doped lanthanum cobalt oxide $(La_{1-x}Sr_xCoO_{3-\delta})$. *Chem. Mater.* **17**, 4537–4546 (2005).
47. Khachaturyan, A. G. *Theory of Structural Transformations in Solids* (Wiley, Hoboken, 1983).
48. Cahn, J. W. & Hilliard, J. E. Free energy of a nonuniform system. I. Interfacial free energy. *J. Chem. Phys.* **28**, 258–267 (1958).
49. Freedman, D. A., Roundy, D. & Arias, T. A. Elastic effects of vacancies in strontium titanate: short- and long-range strain fields, elastic dipole tensors, and chemical strain. *Phys. Rev. B* **80**, 064108 (2009).
50. Levanyuk, A. P., Minyukov, S. A. & Cano, A. Universal mechanism of discontinuity of commensurate-incommensurate transitions in three-dimensional solids: strain dependence of soliton self-energy. *Phys. Rev. B* **66**, 014111 (2002).
51. See supplementary materials at (URL to be provided by the publisher).
52. Morozovska, A. N. *et al.* Phase diagrams and domain splitting in thin ferroelectric films with incommensurate phases. *Phys. Rev. B* **81**, 195437 (2010).

Acknowledgements

Author contributions

A.N.M. and Y.A.G. generated the research idea, stated the problem, and performed analytical calculations jointly with E.A.E. E.A.E. wrote the codes and performed numerical calculations. A.N.M., S.V.K and Y.A.G. wrote the manuscript draft. All co-authors worked intensively on the results interpretation and manuscript improvement.

Funding

Competing interests

The authors declare no competing interests.

Additional information

Supplementary Information The online version contains supplementary material available at https://doi.org/10.1038/s41598-020-79482-w.

Correspondence and requests for materials should be addressed to S.V.K. or Y.A.G.

Reprints and permissions information is available at www.nature.com/reprints.

Publisher's note Springer Nature remains neutral with regard to jurisdictional claims in published maps and institutional affiliations.